Eur Biophys J (2003) 32: 689–702
DOI 10.1007/s00249-003-0330-y

ARTICLE

**Assen Koumanov · Ulrich Zachariae**
**Harald Engelhardt · Andrey Karshikoff**

# Improved 3D continuum calculations of ion flux through membrane channels

Received: 19 February 2003 / Revised: 14 May 2003 / Accepted: 16 May 2003 / Published online: 18 July 2003


**Abstract** A continuum model, based on the Poisson–Nernst–Planck (PNP) theory, is applied to simulate steady-state ion flux through protein channels. The PNP equations are modified to explicitly account (1) for the desolvation of mobile ions in the membrane pore and (2) for effects related to ion sizes. The proposed algorithm for a three-dimensional self-consistent solution of PNP equations, in which final results are refined by a focusing technique, is shown to be suitable for arbitrary channel geometry and arbitrary protein charge distribution. The role of the pore shape and protein charge distribution in formation of basic electrodiffusion properties, such as channel conductivity and selectivity, as well as concentration distributions of mobile ions in the pore region, are illustrated by simulations on model channels. The influence of the ionic strength in the bulk solution and of the externally applied electric field on channel properties are also discussed.

**Keywords** Current–voltage characteristics · Ion solvation · Poisson–Nernst–Planck theory · Protein channels

## Introduction

Different computational approaches are currently applied for prediction and analysis of electrophysiological properties of membrane channels. It appears to be a common opinion that the most rigorous methods are the "direct" (Levitt 1999) approaches, such as molecular dynamics (MD) and Brownian dynamics (BD) simulations (Levitt 1999; Tieleman et al. 2001; Roux 2002). Electrodiffusion models based on the Poisson–Nernst–Planck (PNP) theory are also widely used for calculation of ion current through membrane channels (Eisenberg 1996). The PNP models are often subject of criticism and in some cases it reaches a level at which, besides the large computational demands of MD and BD, no room for justification of the PNP approach is left (Levitt 1999). A weakness of this approach is that, being a continuum model, the specific interactions of mobile ions with the channel lining are not considered accurately. Also, the properties of water in the channel are represented by adjustable parameters. The difficulties of the PNP method become evident when narrow channels are investigated. It has been illustrated that in these cases PNP breaks down (Dieckmann et al. 1999; Corry et al. 2000, 2001). Graf et al. (2000) and others (Corry et al. 2000, 2001) have pointed out that one of the problems of the PNP approach is the omission of the desolvation of the mobile ions in the pore region.

The use of averaged theories, such as PNP, has been well justified for the investigation of processes, like measurable ion permeation through channels, which involve a large amount of atoms and have a long (on an atomic time scale) duration (Eisenberg 1996; Noner et al. 1999). Thus, electrodiffusion models supplied with appropriate, physically grounded parameters are, in principle, capable not only of fitting a vast range of experimental data but also of providing a reliable insight into the major factors governing ion conductivity of channels. Nonner and Eisenberg (1998) extended the basic one-dimensional PNP theory by adding excess chemical potentials simply as parameters accounting for all effects not included in the mean electrostatic potential. After calibration (the values of the diffusion coefficients and the excess chemical potentials inside the selective filter were determined from several measurements), the new model (called

A. Koumanov (✉) · A. Karshikoff
Department of Biosciences at Novum,
Karolinska Institute, 14157 Huddinge, Sweden
E-mail: assen.koumanov@csb.ki.se
Tel.: +46-8-6083305
Fax: +46-8-6089290

U. Zachariae · H. Engelhardt
Abteilung Molekulare Strukturbiologie,
Max-Planck-Institut fuer Biochemie,
Am Klopferspitz 18a, 82152 Martinsried, Germany

there PNP2) accurately predicted a big variety of observed properties of the L-type Ca channel. However, as the authors have pointed out, the atomic origin of the values used for the calibrated parameters remains unclear. In a subsequent paper (Nonner et al. 2000), considering the same channel at equilibrium, the excess chemical potentials of ions in bulk and in the filter were calculated by applying the mean spherical approximation (MSA). The main results of this study were confirmed by Boda et al. (2000, 2001), who used canonical Monte Carlo simulations utilizing the same representation of the electrolyte (hard-sphere ions and continuum water). The simulations showed that the channel selects cations with higher valence and among equally charged ions the permeation of the smaller ones is favoured. Thus, the selectivity of $Ca^{2+}$ over $Na^{+}$ was explained as a result of charge/space competition. Goulding et al. (2000, 2001) examined the penetration of hard spheres (ions and water molecules) into pores with simple shapes by density functional theory and grand-canonical Monte Carlo simulations. These studies highlight the significance of the entropy effects for selectivity of narrow confined volumes. It was also shown that in a cylindrical channel, at specific ratios between radii of the pore and the solution particles, the absorption of larger particles may be preferable. Recently, Nonner et al. (2001) extended their MSA-based approach by treating the water not as a continuum but as uncharged hard spheres and by allowing the volume of the filter to change under the solvent pressure, resulting in mechanical work on the protein.

All studies discussed in the previous paragraph are lacking a rigorous consideration of how the dielectric boundary charge induced by the mobile ions influences their motion. Schuss et al. (2001) derived a coupled system of Poisson and Nernst–Planck equations describing ion permeation through channels. In the new form of the PNP equations the effect of dielectric boundaries is properly taken into account, so that one major disadvantage of the method is eliminated. Two alternative algorithms [based on spectral element and conjugated gradient techniques (Hollerbach et al. 1999, 2000) and respectively on finite difference (FD) and successive over-relaxation (SOR) methods (Kurnikova et al. 1999; Cardenas et al. 2000)] for computing three-dimensional solutions of the PNP equations were proposed and applied to the gramicidin A channel. Thus, another strong simplification of the PNP approach, largely implemented before, has been avoided, namely the reduction of the task from three- to one-dimensional. The good agreement between the theoretical and experimental results, reported in these papers, is very encouraging and suggests once again that that the continuum model is an appropriate tool for analysis of membrane channels.

Continuum models allow, to certain limits, the introduction of atomic details. Such combined models are successfully used in different areas of physical chemistry. For instance, the "macroscopic electrostatic with atomic details" model [MEAD (Dillet et al. 2000)] predicts the ionization constants of titratable groups in proteins sufficiently well. The introduction of some components of side-chain conformational flexibility (Alexov and Gunner 1997; Gunner and Alexov 2000), as well as the pH dependence of proton allocations on titratable and polar groups (Koumanov et al. 2002, 2003), are other examples of combining continuum models with properties on an atomic level. This, together with the above-mentioned recent theoretical and computational achievements in the investigations of ion channels, stimulated us to rewrite our FD solver (Karshikoff 1995; Koumanov et al. 2003) to enable a self-consistent solution of the Poisson and Nernst–Planck equations.

In this study we propose an FD-based algorithm for calculation of PNP equations. Unlike the approach of Kurnikova and co-workers (Kurnikova et al. 1999; Cardenas et al. 2000), our method takes into account the effect of desolvation of the mobile ions in the membrane pore, as well as some effects related to ion sizes. In addition, a focusing technique was applied to achieve a finer FD grid with improved boundary conditions. The algorithm showed stable relaxation of the numerical solution for channels with different size, shape and charge composition.

## Methods

### Continuum model

The model used for calculations of the $I$–$V$ characteristics of ion channels is illustrated in Fig. 1. The solvent is represented as a medium with a permittivity, $\epsilon_s$ (for instance, the dielectric constant of water), which contains $n$ species of mobile ions treated as a continuum matter, hence described by the space distributions of their local concentration, $c_i(\boldsymbol{r}), i = 1, ..., n$. Ion types are characterized by their charges, $Z_i e$, diffusion coefficients, $D_i(\boldsymbol{r})$, and radii, $R_i$. The latter define ion inaccessible regions around the membrane and the protein (i.e. the ion exclusion volume, $V^{exc}$). The membrane is represented as a planar layer with a certain thickness in which the protein molecule is immersed. Both the membrane and the protein are considered as materials with appropriate dielectric constants (Fig. 1), which is impenetrable for the solvent and the mobile ions. In this way, the solvent is separated by the membrane into two bath regions, which can exchange ions only through the protein channel. The channel shape and dimensions are defined by the 3D protein structure and the van der Waals radii of the protein atoms. The protein possesses also a charge distribution, $\rho_p(\boldsymbol{r})$, determined by its structure and ionization state. The ion concentrations in the reservoirs on both sides of the membrane may be different, i.e. $C'_i \neq C''_i$, and an external voltage, $V''-V'$, can be applied.

In order to achieve a more realistic representation of the protein–membrane–solvent system, the algorithm was constructed to allow assignment of individual dielectric constants to different regions of the membrane and to different parts of the protein molecule. Similarly, individual values for the ion diffusion coefficients and for the permittivity can be assigned to different regions of the solvent.

As shown in Fig. 1, the membrane can be composed of three sub-layers, each having an appropriate thickness and permittivity. The regions with dielectric constant $\epsilon_{pm}$ correspond to polar lipid head groups (Karshikoff et al. 1994; Zachariae et al. 2002), whereas the aliphatic core is characterized by a dielectric constant $\epsilon_{am}$, and

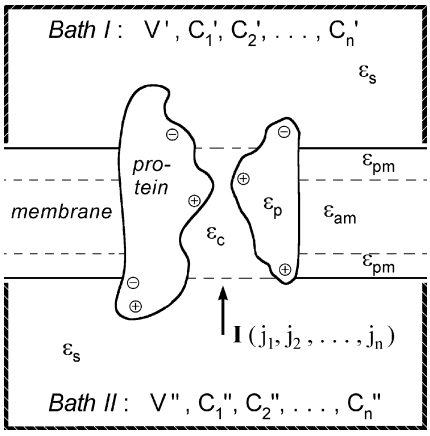


**Fig. 1** Schematic representation of the model used for calculations of ion fluxes through membrane channels. The system of interest is situated in a *cubic box*. The solvent with permittivity, $\epsilon_s$, is separated by an impermeable membrane into two infinite reservoirs (*Bath I* and *Bath II*) containing $n$ species of mobile ions with concentrations $C'_1$, $C'_2$, ..., $C'_n$ and $C''_1$, $C''_2$, ..., $C''_n$, respectively. Electrostatic potentials $V'$ and $V''$ of the baths are used to simulate a transmembrane voltage of $V''-V'$. A protein molecule with certain charge distribution and dielectric constant $\epsilon_p$ forms an ion permeable channel through the membrane. The permittivity of the channel interior $\epsilon_c$ can be set different from $\epsilon_s$, and membrane slabs with permittivities $\epsilon_{pm}$ and $\epsilon_{am}$ can be defined to account for polar and aliphatic parts of a lipid bilayer. The electric current, $I$, resulting from ion fluxes $j_1$, ..., $j_n$ through the channel is the subject of calculations. The boundary surface of the computational box through which ion exchange with the infinite reservoirs occurs is given with a *thick line*

may differ from that of the protein. The algorithm also allows assignment of different dielectric constants to different parts of the protein molecule (Voges and Karshikoff 1998). It is also straightforward to add surface densities of dipoles and/or charges on the membrane–solvent interface if necessary (Cardenas et al. 2000). A list of all physical parameters used in the calculations is given in Table 1.

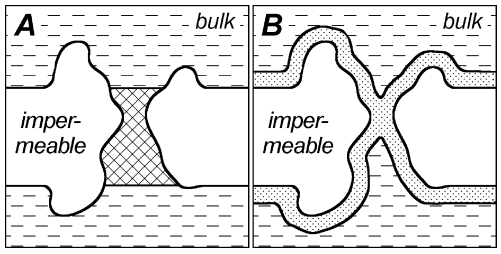


**Fig. 2** Diffusion coefficients and dielectric constant, different from those of the bulk solvent, can be assigned to (**A**) the channel interior and (**B**) solvent strata with certain thicknesses wrapping the permeable–impermeable boundary surface. For survey purposes the algorithm allows combination of both mapping schemes

The properties of bulk solutions are well-studied and high-quality experimental data are available for the permittivity, $\epsilon_s$, of water as well as for the diffusion coefficients of a vast variety of ion species. However, close to protein–solvent and membrane–solvent boundaries, water may exhibit properties essentially different from those in the bulk. It is then reasonable to assume that the values of $\epsilon_s$ and $D_i$ in the region of the solvent–membrane interface and in the channel interior differ from those in the bulk. To our knowledge, there are no direct experimental measurements of such boundary values. It has been suggested by other authors that in channels the permittivity is 2- to 4-fold (Partenskii and Jordan 1992; Sansom et al. 1997) and the diffusion coefficients are 2- to 10-fold (Tieleman and Berendsen 1998; Smith and Sansom 1999; Allen et al. 2000) lower than the corresponding values of the bulk. To reflect this, two zones of the solvent with specific non-bulk properties were introduced in the model. The first one is in the channel interior (Figs. 1, 2A) and the second zone corresponds to a stratum wrapping accessible surface for ions of type $i$, where a particular value of $D_i$ can be specified (Fig. 2B).

## Theoretical background

In the continuum approach ions are treated as Brownian particles, the dynamics of which is described by the Smoluchowski equation:

**Table 1** List of physical parameters defining the ion fluxes through a protein channel represented by a continuum model. Values are given for the test system used in assessment of precision and accuracy of the FD solution of the PNP equations

| Quantities | Notation | Value(s) |
|---|---|---|
| Coordinates, radii, partial charges, inhomogeneous permittivity (assigned to protein atoms) | | From files |
| Supplementary potential maps | $\phi_k{}^m$, $\phi'_k{}^k$ | From files |
| Temperature | $T$ | 293.15 K |
| Membrane thickness | | 36 Å |
| Thickness of polar membrane sub-layers: upper, lower | | 0 Å, 0 Å |
| Membrane pore radii: upper, middle, lower | | 10 Å, 4 Å, 10 Å |
| Permittivities of membrane sub-layers: polar, aliphatic | $\epsilon_{pm}$, $\epsilon_{am}$ | 40, 4 |
| Solvent permittivities: bulk, channel interior | $\epsilon_s$, $\epsilon_c$ | 80, 80 |
| Solvent probe radius | | 1.4 Å |
| Protein–solvent dielectric boundary | | No smoothing |
| Number of ion species | $n$ | 2 |
| Ion charges | $Z_i e$ | $+1e$, $-1e$ |
| Ion radii | $R_i$ | 1.5 Å, 1.5 Å |
| Thickness of solvent layers with boundary ion diffusion coefficients | | 2.8 Å, 2.8 Å |
| Diffusion coefficients for ion species: | $D_i$ | |
| in bulk | | $10^{-5}$ cm$^2$/s, $10^{-5}$ cm$^2$/s |
| in channel interior | | $10^{-5}$ cm$^2$/s, $10^{-5}$ cm$^2$/s |
| in boundary region (close to ion-accessible surface) | | $10^{-5}$ cm$^2$/s, $10^{-5}$ cm$^2$/s |
| Bath I (upper): electric potential, ion concentration | $V'$,$C'_i$ | −25 mV, 0.01 M, 0.01 M |
| Bath II (lower): electric potential, ion concentration | $V''$,$C''_i$ | +25 mV, 0.01 M, 0.01 M |

$$\frac{\partial c(r,t)}{\partial t} = -\nabla \mathbf{j}(r,t) \tag{1}$$

where $c(\boldsymbol{r},t)$ is the particles' concentration at location $\boldsymbol{r}$ and at moment $t$. Their flux, $\mathbf{j}(r,t)$, is given by:

$$\mathbf{j}(r,t) = -D(r)\Big(\nabla c(r,t) + (kT)^{-1}c(r,t)\nabla U(r)\Big) \tag{2}$$

Here, and further on, $D$ denotes the diffusion coefficient, $k$ and $T$ are the Boltzmann constant and the absolute temperature, respectively, and $U(\boldsymbol{r})$ represents the potential energy of a single particle placed at location $\boldsymbol{r}$, i.e. $-\nabla U(\boldsymbol{r})$ is the external force acting on this particle. In steady state, where $(\partial c/\partial t = 0)$, Eqs. (1) and (2) give the Nernst–Planck (NP) equation for ions of type $i (i = 1 \ldots n)$:

$$\nabla\Big[D_i(r)\Big(\nabla c_i(r) + (kT)^{-1}c_i(r)\nabla U_i(r)\Big)\Big] = 0 \tag{3}$$

Each Eq. (3) has a unique solution in an arbitrary volume if $D_i(\boldsymbol{r})$ and $U_i(\boldsymbol{r})$ are known for the entire volume and $c_i(\boldsymbol{r})$ are given at the boundary surface. Once obtained, the ion concentration distributions can be used in Eq. (2) to calculate the corresponding fluxes, which multiplied by $Z_i e$ and integrated over a cross-section of the channel yield the electric current.

The potential energy of an ion of species $i$ at point $\boldsymbol{r}$, $U_i(\boldsymbol{r})$, may comprise components of different physical origin. We assume that these components are additive and mutually independent:

$$U_i(r) = U_i^{\mathrm{el}}(r) + U_i^{\mathrm{sol}}(r) + U_i^{\mathrm{other}}(r) \tag{4}$$

where $U_i^{\mathrm{el}}(\boldsymbol{r})$ is the electrostatic energy of the interaction of an ion with the external voltage, the permanent charges of the channel lining molecule(s) and all other ions in the solvent. $U_i^{\mathrm{sol}}(\boldsymbol{r})$ is the ion solvation energy. All interactions and effects not described by these two terms are formally represented by $U_i^{\mathrm{other}}(\boldsymbol{r})$, which, in this study, is limited to a hard-core potential as an approximation of the van der Waals interactions, in which a probe ion participates. This potential, reflecting the finite size of the mobile ions, is further introduced into the PNP equations implicitly by simple geometrical considerations. In general, the content of $U_i^{\mathrm{other}}(\boldsymbol{r})$ can be extended by some components of the excess chemical potential (see end of this subsection).

It follows from the hard-spheres approximation that if point $\boldsymbol{r}_0$ is occupied by an ion of type $i$, an ion of type $j$ can not be closer to $\boldsymbol{r}_0$ than $R_i + R_j$, i.e. $c_j(\boldsymbol{r}) \equiv 0$ if $|\boldsymbol{r}_0 - \boldsymbol{r}| < R_i + R_j$. In this way, unlike the standard continuum approach, ions are treated (at least locally) as discrete particles with non-negligible size, which is in fact an introduction of a new atomic detail in the continuum model. To obtain the electrostatic part of the potential acting on ion species $i$ at point $\boldsymbol{r}_0$, $U_i^{\mathrm{el}}(\boldsymbol{r}_0)$, we use the mean-field approximation in the sense that all ions, except a hypothetical one located at $\boldsymbol{r}_0$, are represented by their concentrations $c_j(\boldsymbol{r})$. Hence, $U_i^{\mathrm{el}}(\boldsymbol{r}_0)$ can be written as $U_i^{\mathrm{el}}(\boldsymbol{r}_0) = Z_i e \psi_{i,\boldsymbol{r}0}(\boldsymbol{r}_0)$, where the electrostatic potential, $\psi_{i,\boldsymbol{r}0}(\boldsymbol{r})$, is the solution of the following Poisson equation:

$$-\nabla(\varepsilon(r)\nabla\psi_{i,r_0}(r)) = 4\pi[\rho_{\mathrm{p}} + \sum_j Z_j e \gamma_j(r) c_j(\mathbf{r}|_{|r-r_0|\geq R_i+R_j})]_{\psi_{i,r0}(\mathrm{boundary})=f(V',V'')} \tag{5}$$

Here, ion concentrations (charges) within vicinities of $\boldsymbol{r}_0$, $|\boldsymbol{r}_0 - \boldsymbol{r}| < R_i + R_j$, are "removed" and do not act as a source of potential, which is equivalent to the restriction $c_j(\boldsymbol{r}|_{|\boldsymbol{r}0\text{-}\boldsymbol{r}| < Ri + Rj}) \equiv 0$. The externally applied voltage is introduced through the boundary conditions. The factor $\gamma_j(\boldsymbol{r})$ rescales the value of concentration in the vicinity of the ion-inaccessible boundary and is related to the ion size. This is essential for confined spaces with volumes comparable to that of a single ion, e.g. narrow channels. For instance, let us consider a closed volume $V$ containing $N$ ions with some radius $R \neq 0$. Their concentration is defined simply as $c = N/V$ and the volume accessible for the centers of the mobile ions is $V^{\mathrm{acc}} = V - \mathrm{V}^{\mathrm{exc}} < V$. If the number of ion centers, $N'$, is calculated as $N' = cV^{\mathrm{acc}}$, it follows that $N' < N$, which is obviously incorrect. The local distortions in counting the number of ions are formally corrected by the factor $\gamma_j(\boldsymbol{r})$ defined as $\gamma_j(\boldsymbol{r}) v_j^{\mathrm{acc}}(\boldsymbol{r}) = v_j$, where $v_j$ is the total volume of ion $j$ and $v_j^{\mathrm{acc}}(\boldsymbol{r})$ is that part of the volume of ion $j$, placed at point $\boldsymbol{r}$, which is also part of the ion accessible space. If the distance from point $r$ to the ion accessible surface is larger than the ion radius, then $\gamma_j(\boldsymbol{r}) = 1$, or $\gamma_j(\boldsymbol{r}) > 1$ otherwise. For infinitesimal ions (ions considered as points), $\gamma \equiv 1$.

It should be mentioned that, according to Eq. (5), the reaction field of the dielectric induced by the hypothetical ion placed at point $\boldsymbol{r}_0$ is in fact excluded from $U_i^{\mathrm{el}}(\boldsymbol{r}_0)$. In this work, the reaction field of the dielectric is accounted for separately via Eq. (4), where the solvation term, $U_i^{\mathrm{sol}}(\boldsymbol{r}_0)$, is given by Eq. (9) (below). It is convenient to represent the potential $\phi_{i,\boldsymbol{r}0}(\boldsymbol{r}_0)$ as a sum of electrostatic potentials created from different sources, so that $U_i^{\mathrm{el}}(\boldsymbol{r}_0)$ can be written as:

$$U_i^{\mathrm{el}}(r_0) = Z_i e\left[\varphi(r_0) - \sum_{j=1}^{n} Z_j \Big(\int_{V_j} \varphi_{r_0}(r)\gamma_j(r)c_j(r)\,\mathrm{d}v\Big)\right] \tag{6}$$

where the integrations are over spherical volumes $V_j$ centred at $\boldsymbol{r}_0$ and having corresponding radii $R_i + R_j$. The electrostatic potentials $\phi(\boldsymbol{r})$ and $\phi_{\boldsymbol{r}0}(\boldsymbol{r})$ satisfy the following Poisson equations:

$$-\nabla(\varepsilon(r)\nabla\varphi(r)) = 4\pi[\rho_{\mathrm{p}}(r) + \sum_j Z_j e \gamma_j(r) c_j(r)]_{|\phi(\mathrm{boundary})=f(V',V'')} \tag{7}$$

$$-\nabla(\varepsilon(r)\nabla\phi_{r_0}(r)) = 4\pi e\delta(r - r_0)_{|\phi_{r_0}(\mathrm{boundary})\equiv 0} \tag{8}$$

In Eq. (8), $e\delta(\boldsymbol{r} - \boldsymbol{r}_0)$ indicates placement of a unit point charge at $\boldsymbol{r}_0$. Equation (7) is, in fact, the Poisson equation for the mean-field electrostatic potential $\phi(\boldsymbol{r})$ of the entire considered system. In some other PNP approaches (e.g. Kurnikova et al. 1999; Cardenas et al. 2000), all the electrostatic components of $U_i(\boldsymbol{r})$ are represented solely by $\phi(\boldsymbol{r})$.

The desolvation penalty for transferring an ion from the bulk solution to the vicinity of the membrane or the protein molecule is taken into account explicitly via the solvation energy term $U_i^{\mathrm{sol}}(\boldsymbol{r})$ in Eq. (4). The assumption for independency of the components of $U_i(\boldsymbol{r})$ allows the solvation term, $U_i^{\mathrm{sol}}(\boldsymbol{r})$, to be introduced independently of the PNP theory. In this study the solvation energy is considered as the difference in self-energy of an ion in position $\boldsymbol{r}$, $U_i^{\mathrm{self}}(\boldsymbol{r})$, and the self-energy of this ion in some reference position (e.g. in the bulk solution), $U_i^{\mathrm{self}}(\mathrm{ref})$, i.e.:

$$U_i^{\mathrm{sol}}(r) = U_i^{\mathrm{self}}(r) - U_i^{\mathrm{self}}(\mathrm{ref}) = Z_i^2 e \phi'_{\mathrm{r}}(r)/2 - U_i^{\mathrm{self}}(\mathrm{ref}) \tag{9}$$

Since, according to Eq. (3), only the differences in solvation energies are relevant, the choice of a reference position is, in fact, arbitrary and there is no need to calculate $U_i^{\mathrm{self}}(\mathrm{ref})$. The potential $\phi'_{\mathrm{r}}(\boldsymbol{r})$ is the solution of Eq. (8), but with non-zero boundary conditions. The desolvation penalty, as defined by Eq. (9), reflects just the changes in the reaction field of the dielectric upon moving a single ion. Effects due to rearrangements and cooperative motions of counterions and/or water molecules in the vicinity of an ion penetrating the channel are excluded from our considerations. An inclusion of such effects is, in principle, possible (if reasonable assessments can be provided for non-equilibrium systems), but it will violate the independency from other terms in Eq. (4) and thus will require more complicated iterative solutions. Moreover, it was shown (Moy et al. 2000) that, for biologically relevant channel dimensions and solutions, the single-ion approximation gives good estimates (in any case better than the Poisson–Boltzmann estimates) of the ion desolvation.

The proposed above modifications of the PNP equations are in fact a substantial refinement in the representation of the electrostatic forces acting on the solution ions. With respect to works employing excess chemical potential in addition to the mean electrostatic field (Nonner and Eisenberg 1998; Gillespie and Eisenberg 2002), these modifications can be viewed as particular contributions to the excess chemical potential. It should be stressed that the approach described here utilizes a hard-sphere model of ions locally,

so that it accounts only for first-order effects related to ion sizes and a priori omits others, such as entropic contributions due to filling the confined space of the channel with ions and water molecules of finite sizes (Goulding et al. 2000, 2001; Nonner et al. 2000, 2001). Entropic and excluded volume effects as well as other effects [e.g. due to specific, not accounted by $U_i^{el}(\boldsymbol{r})$ and $U_i^{sol}(\boldsymbol{r})$, ion–ion, ion–water and ion–protein interactions] can be incorporated in the continuum model through $U_i^{other}(\boldsymbol{r})$ (Eq. 4). This term may be used, for instance, to describe the non-electrostatic components in ion binding affinities to a specific protein site. The anomalous mole fraction effect was analysed by assuming that two equally charged ion species possess different binding affinities of to certain loci of a model channel (Nonner et al. 1998). Extension of the content of $U_i^{other}(\boldsymbol{r})$ is equivalent to inclusion of those parts of the excess chemical potential, which are not accounted by the first two terms in Eq. (4). Most often, the excess chemical potential is evaluated empirically from some experimental data; however, such strategy has never been attempted in 3D work.

## Finite difference solution of the PNP equations

For an arbitrary channel shape, Eqs. (3), (4) and (6, 7, 8, 9) can be solved numerically, for instance by means of the FD technique, well known and widely used for calculations of protein electrostatics (Warwicker and Watson 1982; Nicholls and Honig 1991). According to this method, the system of interest is represented by a cubic grid box and the quantities characterizing the system are assigned to each grid point. The values of these quantities are either defined by the concrete model (diffusion coefficients, dielectric constants, permanent charges, etc.) or are subject of calculations (ion concentrations, electric potential). Calculations are performed in the interior of the grid cube, while the values at the points belonging to the box walls are defined by the boundary conditions.

For any internal point $k$ the FD representation of Eq. (3) gives:

$$c_i^k \sum_j (1-\alpha_i^{jk})\bar{D}_i^{jk} - \sum_j (1+\alpha_i^{jk})\bar{D}_i^{jk} c_i^j = 0$$
$$\alpha_i^{jk} = (U_i^j - U_i^k)/2kT, i = 1,2,...,n, \qquad (10)$$

where subscript and superscript indexes designate the ion species and the grid points, respectively. The summations are over the six grid points neighbouring point $k$. $\bar{D}_i^{jk}$ is the effective diffusion coefficient describing the ion exchange between the $k$-th and $j$-th points. It is defined as $\bar{D}_i^{jk} = (D_i^k + D_i^j)/2$ if both points, $j$ and $k$, are accessible for the $i$-th ion type ($D_i^k$ and $D_i^j$ are the diffusion coefficients for ions $i$ at points $k$ and $j$, respectively), and $\bar{D}_i^{jk} = 0$ otherwise (formally representing the absence of ion exchange). The ion concentration, $c_i^k$, is calculated if point $k$ is accessible for the $i$-th ion type, otherwise it is set to zero. Protein cavities that are unable to exchange ions with the bulk are considered as ion-inaccessible regions.

Depending on the field $U_i$ and on the grid size, it may occur that the first sum in Eqs. (10) turns to zero or the two sums have different signs. In the first case, the value of $c_i^k$ is indefinite, while the second case suggests an unrealistic, negative concentration. Obviously, if $|\alpha_i^{jk}| < 1$ for all $\alpha_i^{jk}$, such problems will be discarded a priori. This condition can be fulfilled by reducing the grid spacing, $h$, at the expense of computing efficiency. Here, this problem was approached by applying a restriction on potential gradients, namely, if $|U_i^j - U_i^k| \geq 2kT$, then $\alpha_i^{jk}$ is set either to $+\xi_i$ or to $-\xi_i$, where $0 < \xi_i < 1$ are truncation parameters (in our calculations, $\xi_i = 0.99$) and the sign is chosen to coincide with the sign of $(U_i^j - U_i^k)$. Such a truncation of the potential gradients is of course a local violation of the NP equations. However, it allows computations in cases where the exact Eqs. (10) fail (for example, highly charged protein sites on the channel wall combined with a low permittivity of the channel interior). Test calculations showed first that, in the final solution of the PNP equations, the number of truncations is negligible in comparison with the total amount of grid points in the channel, and second that these local violations of NP equations have weak propagation (the values of concentrations are practically affected only at the nearest neighbouring points). Thus, in the majority of the cases, the calculated total electric current is insensitive to the gradient truncations. Similar issues were addressed in stationary drift-diffusion simulations of semiconductor devices (Sartoris 1998).

The potential, $U_i^k$, of an ion of type $i$ at grid point $k$ can be expressed in FD terms as:

$$U_i^k = Z_i e\left[\phi^k - h^3 \sum_{j=1}^{n} Z_j \left(\phi_k^{mj} \gamma_j^{mj} c_j^{mj}\right) + Z_j \phi_k'^k/2\right] \qquad (11)$$

where the first summation is over all ion species, the second summation is over all grid points for which $|km_j| < R_i + R_j$ and $h$ is the grid spacing. The FD formula for the potential $\phi^k$(Eq. 7) at grid point $k$ can be written as follows:

$$\varphi^k = \frac{\sum_j \bar{\varepsilon}^{jk}\phi^j}{\sum_j \bar{\varepsilon}^{jk}} + \frac{4\pi[q_p^k + h^3 \sum_i Z_i e \gamma_i^k c_i^k]}{h \sum_j \bar{\varepsilon}^{jk}} \qquad (12)$$

The term in square brackets represents the charge assigned to point $k$(resulting either from permanent charges or from the ion content) and $\bar{\varepsilon}^{jk}$ equals the arithmetic average of the permittivities $\epsilon^k$ and $\epsilon^j$ characterizing $k$-th and $j$-th points, respectively.

The electrostatic potentials $\phi_k{}^m$ and $\phi'_k{}^k$ in Eq. (11) are discrete representations of $\phi_{r0}(\boldsymbol{r})$ and $\phi'_r(\boldsymbol{r})$, respectively. The subscript indexes denote the location of the unit charge (source of the corresponding potential) and superscripts indicate grid points where values of the potentials are taken. It is evident from Eq. (8) that both $\phi_k{}^m$ and $\phi'_k{}^k$ depend only on the dielectric environment and can be calculated independently. In the proposed algorithm, the PNP equations are represented by Eqs. (10, 11, 12), where $\phi_k{}^m$ and $\phi'_k{}^k$ are preliminary calculated. Rigorously, the preliminary computations require an FD solution of a Poisson equation for each particular placement of a test charge in an ion-accessible grid point. The number of these points is usually of the order of $10^5$–$10^6$, which makes the task prohibitively time consuming. In order to overcome this obstacle we choose a sample of about $10^3$–$10^4$uniformly distributed grid points, in which test charges are placed and corresponding FD calculations are performed. For the remaining grid points, the potentials $\phi_k{}^m$ and $\phi'_k{}^k$ are obtained by an interpolation employing both the values in the sampled points and the local dielectric mapping. This approach was found to provide satisfactory accuracy and precision at a reasonable computational cost.

The non-linear system of equations (Eqs. 10, 11, 12) that has to be solved can be easily decoupled to independent linear systems by fixing the values of $U_i^k$ in Eqs. (10) and the values of $c_i^k$ in Eq. (12). Our algorithm employs SOR as an efficient method for numerical solution of big linear systems (Nicholls and Honig 1991; for review see Hadjidimos 2000). Equations (10, 11, 12) are solved by $n+1$ (for $c_1$, ..., $c_n$ and $\phi$) separate SOR procedures, the parameters of which are regularly updated consistently with the temporary results from all SOR procedures. Thus, Poisson and Nernst–Plank equations are coupled via the updates, and hence a self-consistent solution is achieved in a Gummel iteration (GI) (Gummel 1964; Selberherr 1984; Jerome 1996). Analogous approaches, which can be considered GI, are widely used not only in semiconductor studies but also in other research areas (Riveros et al. 1989; Nicholls and Honig 1991; Eisenberg 1996; Kurnikova et al. 1999; Hollerbach et al. 2000). In our implementation, each GI loop consists of one update of parameters followed by relatively short (20–50 SOR iterations) SOR runs for all of the wanted quantities. At the $m$-th GI step, the electrostatic potential $\phi^{(m)}$ is calculated by using, in Eq. (12), the ion concentrations, $c_i^{(m-1)}$, obtained in the previous iteration step. Then the concentration of the $i$-th ion species at point $k$, $c_i^{k(m)}$, is calculated as:

$$c_i^{k(m)} = \omega_i c_i'^{k(m)} + (1-\omega_i) c_i^{k(m-1)} \qquad (13)$$

where $c'_i{}^{(m)}$ results from SOR runs based on Eqs. (10), in which $\alpha_i^{(m)}$ were determined from $\phi^{(m)}$ and $c_i^{(m-1)}$ through Eq. (11) and

truncated if $|\alpha_i^{jk}| > 1$. The mixing parameters $\omega_i$ ($\omega_i > 0$) are not related to the over-relaxation parameters used in the individual SOR runs and are introduced to ensure the overall convergency. The optimal values of $\omega_i$ depend strongly on the features of the simulated system (ionic strength, distribution of fixed charges, grid spacing, etc.). In our algorithm, the values of the mixing parameters are automatically modified during the computational process, aiming at the best convergency rate ($0.1 < \omega_i^{\text{best}} < 1$, in the calculations presented below). The convergency criterion is based on the quantities' deviations due to the last GI loop as well as on the convergency rate, which guarantees that the final results do not differ from the exact FD solution (an infinite GI) more than certain preliminary chosen parameters.

As a starting point, we set all the potentials and concentrations in the interior of the computational cube to zero and perform several preliminary GI loops with $\omega_i = 1$ and an absolute temperature (see Eqs. 10) 2- to 5-fold higher than that used in the real calculations. More sophisticated, non-zero initial conditions, for instance derived from some simplified equilibrium model [e.g. the "initial guess" proposed by Cardenas et al. (2000)] lead to faster solutions only in the cases where the GI converges rapidly anyway. However, if dozens or even hundreds of GI loop iterations are needed to achieve the final solution, the "initial guess" practically loses its advantage.

Owing to the double summation term in Eq. (11), the proposed above solution of the PNP equations is about twice slower than the standard implementation, which counts only the mean-field potential $\phi$. Also, the preliminary calculation of the potentials ${\phi_k}^m$ and ${\phi'_k}^k$ requires additional computing time. However, as these calculations are sensitive only to the dielectric mapping, they need to be carried out only once for any drift-diffusion simulations not involving changes in $\epsilon(\boldsymbol{r})$, such as analysing $I$–$V$ curves of a given protein channel at different ionic concentrations in bath regions or different distributions of permanent charges.

## Boundary conditions

In order to diminish the influence of the boundary conditions on the solution of the PNP equations, the computational box should be as large as possible (see section on Precision and accuracy) and the membrane channel should be situated in the box center. For simplicity of the algorithm architecture the membrane layer is set perpendicular to the $z$-axis, i.e. parallel to the top and bottom box faces (Fig. 1). On the top and bottom faces, values of the electrostatic potential are fixed to $V'$ and $V''$, respectively, where the difference $V''-V'$ represents the externally applied voltage. Analogously, the ion concentrations on these faces are set equal to the concentrations in the corresponding reservoirs. At ion-accessible areas of the side faces (parallel to the $z$-axis), the potential is kept constant, i.e. it equals either $V'$ or $V''$. Across the membrane, the boundary potential varies linearly along the $z$-axis with a slope accordingly changed if dielectric boundaries are crossed. The ion concentrations on the side walls are assigned according to the Boltzmann distribution counting for changes in the solvation energies in the vicinity of the membrane.

To reduce the inaccuracy of final results caused by inexactness of boundary conditions and at the same time to use a finer grid in the region of interest, we apply a focusing technique widely used in FD calculations of electrostatic potentials (Gilson et al. 1987). That is, we solve the PNP equations consecutively in several cubes, inserted one into another, containing the protein molecule. Boundary and initial values for a given focused box are determined from the previous computational box. Increasing the number of focuses results in an apparent trend of faster convergency and disappearance of grid points for which $|U_i^j - U_i^k| \geq 2kT$.

An important detail in setting boundary values of concentrations for a focused box is that a linear interpolation from the previous grid is not appropriate in the entire computational volume. Close to the membrane, for instance, it may happen that an ion-accessible point from the finer grid is surrounded by coarse grid points, some of which are ion inaccessible. In such cases, ion fluxes at the focused grid point are extrapolated from ion-accessible points of the previous grid and the needed concentration value is then back-calculated from Eq. (10).

To keep consistency of calculations, the potentials ${\phi_k}^m$ and ${\phi'_k}^k$ are obtained separately for each computational box by using a focusing procedure identical to that applied for solving the PNP equations.

## Precision and accuracy of the numerical solution

The final computational outcome depends on the choice of parameters for the numerical solution, such as the number of focusing steps, size, position and spacing of the grids, etc. In order to explore this dependence, a series of calculations were performed on a model channel of 36 Å length, equal to the membrane thickness, and an overall shape of a double funnel with radii 10 Å at the openings and 4 Å in the middle, thus forming a constriction zone. In addition, 40 "atoms" with radii of 1.8 Å were distributed arbitrarily on the channel surface, providing an irregular shape of dielectric and ion-accessibility boundaries. The minimal ion permeable cross-section had an area of $\sim 8$ Å$^2$. Partial charges of $\pm 0.25e$ and $+0.75e$ were assigned to the atoms so that a total permanent charge of $+2e$ was localized in the vicinity of the constriction zone. Dielectric constants of 80 for the solvent and 4 for the membrane layer and the atoms were applied. Two ion species that differ only in the sign of their charges were used. All details for the test calculations are given in Table 1. The effects of desolvation and finite size of mobile ions were ignored in the test calculations.

The electric current, $I$, through the channel was calculated using different cubic grid boxes without focusing. The box edge length, $L$, was varied between 45 Å and 105 Å, while the grid spacing was kept approximately constant ($h \approx 1$ Å). For a given $L$, eight PNP calculations were performed with different mapping of the system onto the grid. The mapping was modified in two ways. First, a difference in mapping is achieved by increasing the number of grid points per edge by one. In this way the reduction of the grid spacing is negligible but the mapping in the region of the channel is significantly changed. Second, the grid was shifted with respect to the channel back and forth along the coordinate axes by 0.5 $h$. Results are represented in Fig. 3 by the mean values of calculated currents (solid line) and the range in which these currents deviate (grey band). As seen from Fig. 3, the current is practically insensitive to the size of the computational volume if the box edge is longer than a certain critical length, $L_c$ ($L_c \approx 60$ Å, in this case). For $L < L_c$, a strong and steady rise of the calculated current was obtained.

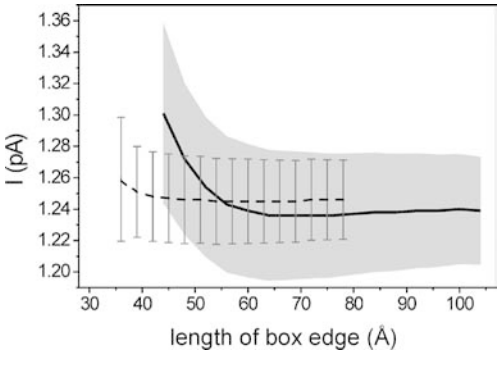


**Fig. 3** Dependence of calculated electric current on the size of the computational box. Initial computations with grid spacing ~1.0 Å were followed by focusing with a grid spacing ~0.75 Å. For each box size, the mapping of the channel onto the grid was varied eight times. Averaged values of currents before (*solid line*) and after focusing (*dashed line*) are shown together with the corresponding variation ranges of these currents (*grey band* and *vertical bars*)

Calculations with finer grids ($h = 0.75$ Å, $h = 0.5$ Å) showed a slight elevation of the mean current and a trend of narrowing the deviation intervals; however, $L_c$ remained around 60 Å (data not shown). This demonstrates that the rise of the current at small computational boxes is due to inadequate boundary conditions and highlights the necessity of sufficiently large initial computational volumes. Variations in the calculated current resulting from changes of the mapping were found to be highly correlated with the corresponding variations in the channel cross-section area as represented by the grid.

Additional simulations revealed that $L_c$ depends on the channel geometry as well as on the ionic strengths in the bath regions. If not only the total current but also the concentration and potential distribution in proximity of the openings are of interest, it is recommended that the length of the initial box, $L_{init}$, satisfies the following two conditions. First, $L_{init} > 1.5l$, where $l$ is the largest dimension of the protein molecule along the coordinate axes. Second, the shortest distance from a protein atom to the box walls should be larger than the Debye length of the nearest bulk region. The last condition is essential at low ionic strength in one or both of the baths.

Calculations were continued with focusing in all boxes with a grid spacing of 1 Å. The results after focusing with $h \approx 0.75$ Å are shown in Fig. 3, together with those from the initial boxes. The plateau level of the mean current after focusing is about 1% higher than the one corresponding to the initial boxes. The deviation interval, which in fact represents the precision of the numerical solution, is twice reduced upon focusing (from ~8% to ~4% of the calculated current). This shows, as expected, that the sensitivity of the calculations to the mapping decreases with reduction of the grid spacing. The elevated values for boxes with $L_{foc} < 40$ Å correspond to the higher current calculated in the preceding boxes ($L < 55$ Å) and originate from the propagation of the initial boundary conditions. It is also notable that results for the smallest focusing boxes ($L_{foc} \approx 35$ Å) are more "noisy". This was found to be caused by a permanent charge that was located very close to or at a boundary face of these focusing boxes. To avoid such numerical artifacts, the walls of the focusing box have to be separated from any permanent charge at least by several grid points. Additional test calculations employing various computational schemes with single, double and triple focusing and with a final grid spacing between 0.6 Å and 0.35 Å were carried out. The average currents of these calculations were found to deviate marginally (< 0.5%) from the plateau level obtained with focusing to $h \approx 0.75$ Å and the final precision was only slightly improved. The difference (~1%) between the average currents obtained with and without focusing provides an estimate of the overall computational accuracy.

In spite of the fact that the features of the focusing technique applied in FD solutions of the Poisson–Boltzmann equation are well documented (Gilson et al. 1987), this method has not been used for the PNP equations. In order to evaluate the accuracy of the focusing procedure itself, the current obtained by a certain focusing scheme was compared to the current calculated in a single box with faces coinciding with those of the initial box used for focusing. In addition, the single box grid had a spacing and disposition identical to that of the finest focusing grid. All comparisons made for a number of different cases showed deviations of less than 0.2%. We also came to the conclusion that the final solution of the PNP equations depends rather on the last mapping used for the calculations (assuming a sufficiently large initial box) than on the features of the preceding grids.

In the converged solutions, two to four potential truncations were present in calculations with $h \approx 1$ Å, while for $h \leq 0.8$ Å potential restrictions were unnecessary.

## Results and discussion

In the following calculations on model channels we evaluate the efficiency of our program with respect to small pores in comparison to the standard PNP approach and demonstrate some basic features of ion transport. In order to facilitate the analysis of results, all simulations were performed for two species of monovalent ions ($Z_{1,2} = \pm 1$) and symmetric bath solutions $C'_{1,2} = C''_{1,2}$. Ion radii of 1.5 Å and diffusion coefficients of $10^{-5}$ cm$^2$ s$^{-1}$ were used. The membrane (thickness = 36 Å) and solvent permittivities were set to 4 and 80, respectively. Channels with three different shapes were studied: cylinder with radius of 4 Å (Fig. 4A), a double-funnel with radii of 10 Å at the openings and 4 Å in the middle (Fig. 4B) and a funnel with a radius of 10 Å in the middle and radii of 4 Å and 16 Å at the openings (Fig. 4C). Computations were carried out for an initial box with 96 Å edge length and 0.8 Å grid spacing, followed by focusing to a box with 48 Å edge length and 0.4 Å grid spacing. FD calculations for sampling self-energy potentials, ${\phi_k}^m$ and ${\phi'_k}^k$, were performed for $9^3$ and $13^3$ grid points of the initial and the focusing boxes, respectively.

### Neutral pores

Figure 4 shows the distributions of ion concentrations and drift velocities in neutral channels calculated for 10 mM ionic strength in the bulk and 100 mV external voltage. The local drift velocity of a given ion species is obtained from its local flux and concentration as:

$$\mathbf{v}_d(r) = \mathbf{j}(r)/c(r) \tag{14}$$

The results clearly demonstrate a non-uniform distribution of ions and their drift velocities in the channel interior. Only a cylindrical channel for which solvation effects are discarded (Fig. 4D, G, J; thin lines) makes an exception of this trend and manifests uniform distributions. For cylindrical and double-funnel pores, the distributions of concentrations and drift velocities of positive (grey lines) and negative ions (black lines) are symmetric to each other (mirror symmetry plane $Z = 0$), which is a direct consequence of the symmetric shape of these channels. Such symmetry of the distributions is lacking in the case of the asymmetric funnel-shaped channel (see Fig. 4F, I, L).

As should be expected, omission of ion solvation energies leads to higher values for the calculated ion content in the membrane pore (Fig. 4D–F, J–L). This weakness of the standard PNP is discussed in detail in other studies comparing the standard PNP approach to BD simulations (Corry et al. 2000; Moy et al. 2000). Among the studied channels, this effect is most pronounced for the cylindrical pore having the smallest volume. Calculations for this pore showed that, along the rotational symmetry axis ($Z$-axis), $c_i$ is 1.5 to 4 times lower than $c_{i(PNP)}$ (Fig. 4D) and at the ion-accessible boundary, i.e. close to the channel walls, $c_i$ is 5 to 20 times lower than $c_{i(PNP)}$. Here and further, quantities obtained by PNP approach, which do not include ion solvation explicitly, are additionally indexed by "(PNP)"

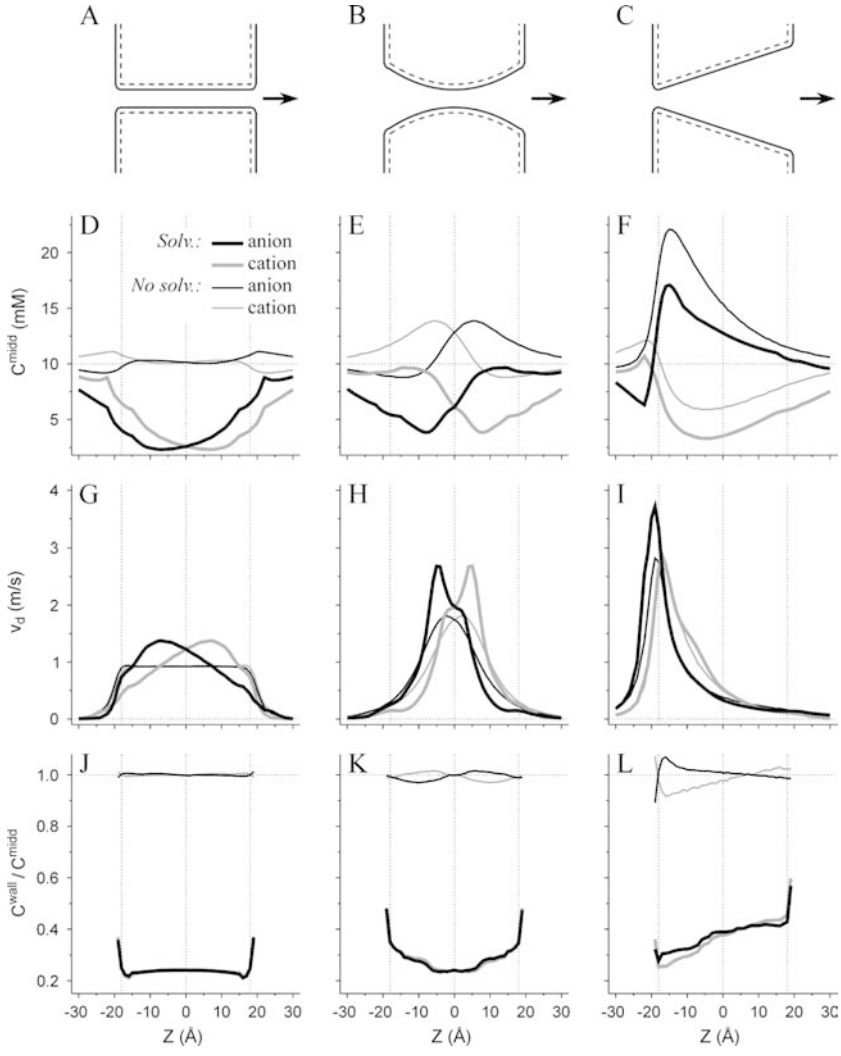


**Fig. 4A–L** Calculated ion concentrations and drift velocities for neutral channels with different shapes. **A–C** Longitudinal cross-sections of a cylindrical, double-funnel and funnel channel. Ion-accessible and dielectric boundary surfaces are marked by *solid* and *dashed lines*, respectively. The direction of the electric current is shown by *arrows*. Longitudinal distribution of: **D–F** ion concentrations in the middle of the channels (along the rotational symmetry axis of the channels), $C^{midd}$; **G–I** absolute values of drift velocities in the middle of the channels; **J–L** ion concentration at the ion-accessible surface of channel interior, $C^{wall}$, relative to $C^{midd}$. *Grey* and *black solid lines* represent quantities for positive and negative ions, while simulations taking into account and those neglecting ion solvation are plotted with *thick* and *thin lines*, respectively. *Vertical dotted lines* indicate the position of the membrane and the channel center. *Horizontal dotted lines* show the bulk ion concentrations (**D–F**), $V_d = 0$ (**G–I**) and $C^{wall} = C^{midd}$ (**J–L**)

in order to be distinguished from quantities (without indexes) calculated by the method proposed in this work (SPNP), where solvation effects are taken into account. A comparison between ion drift velocities obtained by SPNP and by PNP methods (Fig. 4G–I) shows that the maximum of $v_d$ is 20–50% higher than the maximum of $v_{d(PNP)}$. However, drift velocities averaged over the channel interior do not differ essentially, yet $\langle v_d \rangle > \langle v_{d(PNP)} \rangle$. Thus, the ratio of electric currents calculated by the two approaches, $I_{(PNP)}/I$, was found to be 5.2, 3.4 and 1.9 for the cylindrical, double-funnel and funnel pore, respectively. This finding implies that the PNP approach would require significantly lower values for channel diffusion coefficients than the values that would be needed for SPNP to achieve agreement with given experimental data.

Unlike calculations based on PNP, the results from SPNP simulations show distinct radial distribution of ion populations. In any parallel to the membrane cross-section of the channel, ion concentrations decrease from the middle (the intersection with rotational symmetry axis), $C_i^{midd}$, towards the channel walls, reaching its minimum at the ion accessible surface, $C_i^{wall}$. This feature, in fact, reflects the elevation of the desolvation penalty of an ion upon approaching the dielectric boundary of the pore. The ratios $C^{wall}/C^{midd}$, shown in Fig. 4J–L, indicate that the radial distribution of ions inside a channel is determined predominantly by the desolvation effect, while effects related to ion kinetics and polarization caused by the external voltage have only minor contribution. The simulations of Boda et al. (2000) and Goulding et al. (2000, 2001) demonstrate that ions in cylindrical pores have non-trivial radial distributions, which in the many cases show $C^{wall}/C^{midd} > 1$. The discrepancy between their results and ours can be explained by the fact that the SPNP model does not account for entropic effects arising from the arrangement of the ions (hard spheres) in the confined volume of the channel, while their approaches neglect the desolvation. Interestingly, those two effects may produce variations in the radial distributions of approximately the same order. Thus, it is difficult to draw a general conclusion about the radial arrangement of ions inside an arbitrary pore if both the desolvation and the above-mentioned entropic contributions are considered. It should be noted that the results reported

in the studies discussed above do not oppose our basic conclusion for a reduced ion content inside the channel compare to that in the bulk. According to Goulding et al. (2000), the channel to bulk ratio in a concentration of small ions has a maximum of almost 4 at a pore radius of about 3 Å, whereas the desolvation effect, as calculated in our work, leads to more than 10-fold reduction of ion concentration in a channel with the same radius. Thus, the elevated absorbance of the smallest solution particles predicted for some pore sizes will not be able to compensate for the desolvation penalty. Moreover, the SPNP calculations for neutral as well as for charged (see further) channels yield concentration profiles which are in a very good quantitative agreement with the published data from BD simulations (Chung et al. 1998; Dieckmann et al. 1999; Corry et al. 2000, 2001).

## Boundary conditions

All calculations on neutral channels show that, in the bath regions close to the membrane, there is a difference in the concentrations of positive and negative ions. Such differences appear along the membrane as well as at the channel openings (Fig. 4D–F). This leads to accumulation of positive charge in the vicinity of the membrane surface facing the anode (i.e. the membrane side closer to the boundary with higher electrostatic potential) and, analogously, negative charge faces the cathode. This effect, in fact, reproduces the polarization of a solution containing mobile ions on which a permanent external electric field is applied (Robinson and Stokes 1959).

It should be pointed out that the initial boundary conditions do neither imply rigorously the solution polarization caused by the external electric field nor the influence of the membrane pore and ion fluxes through it. In order to illustrate how these simplifications in the boundary conditions affect the calculated distributions of mobile ions and the electrostatic potential, we use a model for which analytical solutions can be derived. The model consists of a pore-less membrane with thickness $d$ and permittivity $\epsilon_m$ embedded in a solution (symmetric baths are used for simplicity) characterized by permittivity $\epsilon_s$ and ionic strength represented by the Debye parameter $\kappa$. Electrodes with applied voltage $V_e$ are placed parallel to the membrane on its both sides, so that solution layers with thickness $L$ are separating the membrane from the electrodes. Ions are considered as point charges and solvation effects are neglected. As far as there are no ion fluxes through the membrane, the system is considered to be in equilibrium, in which case $V_e$ is distributed not only across the membrane but also across the solution layers. Applying the linearized Poisson–Boltzmann equation, one obtains the space distribution of electrostatic potential and hence the potential difference between the membrane surfaces, $V_{mem}$:

$$V_{mem} = V_e \Big/ \left(1 + \frac{4\varepsilon_m \tanh(\kappa L/2)}{\varepsilon_s \kappa d}\right) \tag{15}$$

Apparently, at high ionic strength, $V_{mem} \approx V_e$, while for low ionic strength ($\kappa \to 0$), $V_{mem}$ depends on the ratio $L/d$, i.e. on the concrete geometry. For $\kappa L \gg 1$, which is most often the case in patch-clamp experimental set-ups, Eq. (15) gives $V_{mem} = V_e/(1 + 4\epsilon_m/\epsilon_s \kappa d)$.

The above-described equilibrium system was modelled by formally setting the channel radius and ionic radii to zero and the standard PNP approach was applied to calculate potential and concentrations distributions for bulk ion concentrations of 10 mM and 1 M. All other computational parameters were the same as those used in the flux simulations of neutral channels. These calculations gave for $V_{mem}$ at the $z$-axis (i.e. at the level of the computational box center) values of 94.44 mV and 98.75 mV for salt concentrations of 10 mM and 1 M, respectively. Applying Eq. (15) and assuming large membrane to electrode distances (i.e. $\kappa L \gg 1$), it follows that the above $V_{mem}$ values correspond to $V_e = 110.2$ mV for the lower ion concentration and $V_e = 100.4$ mV for the higher one. Obviously, the boundary potential difference $V'' - V'$ (100 mV in both calculations) does not match exactly the voltage applied on the electrodes. On the walls of the focusing box, numerically calculated distributions of the electrostatic potential (Fig. 5) and ion concentrations (data not presented) agree well with corresponding analytical predictions justified to account for the differences between $V'' - V'$ and $V_e$. It can be concluded that the boundary conditions applied to focusing boxes are indeed much more realistic. The trend of $V'' - V'$ to be an underestimate of $V_e$ is also valid for

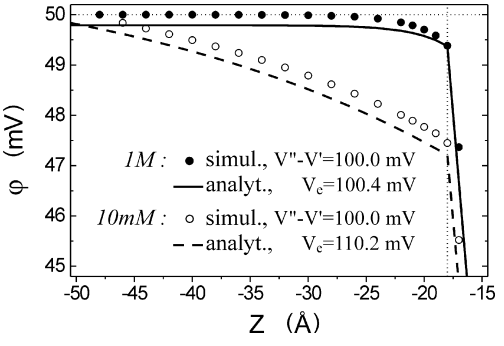


**Fig. 5** Electrostatic potential in the bath region close to the surface of a pore-less neutral membrane embedded in a symmetric solution. FD PNP results using 100 mV potential difference between the faces of the initial computational box ($V' = -50$ mV, $V'' = +50$ mV) and bulk ion concentrations of 10 mM and 1 M are shown with *open* and *filled circles*, respectively. Values are taken from the initial computational boxes along an axis perpendicular to the membrane and lying on one of the side walls of the corresponding focusing boxes. Solvation effects were omitted to allow a straightforward comparison with analytical solutions, represented by: a *dashed line* for 10 mM ionic strength and applied on the electrode voltage $V_e = 110.2$ mV; a *solid line* for 1 M ionic strength and $V_e = 100.4$ mV. The *vertical* and the *horizontal dotted lines* show the membrane-solvent contact and the boundary potential $V''$

SPNP simulations, i.e. when ion sizes and solvation energies are accounted for. Thus, values of $V''$ and $V'$ should be appropriately chosen if computational results are compared to experimental observations, especially if low ionic strengths are of interest. A more rigorous approach would be to set the boundary conditions (both for the electrostatic potential and for the concentrations) according to preliminary calculations, employing either analytical solutions for a simplified model or 1D PNP (or SPNP) equilibrium simulations. The boundary conditions problem is thoroughly explored by Gillespie and Eisenberg (2001). In the present study, as far as no comparison with experimental data was attempted, simple boundary potentials (as described previously in the text) were used and no adjustments towards a hypothetical $V_e$ were made.

## Charged pores

In order to explore the contribution of fixed charges to channel electrodiffusion properties, a unit positive charge was distributed in a ring around the center of each of the three pores shown in Fig. 4A–C. The rings were set parallel to the membrane layer and located inside the membrane, 1 Å away from the channel lining. This simple choice of fixed charges allows us to clearly distinguish their role in the electrodiffusion process. SPNP and PNP calculations were performed and some general trends, similar to those observed for neutral channels, were found. The omission of ion solvation energies again leads to an overestimation of both ion content of the channel and total electric current.

Figure 6 shows distributions of electrostatic potentials along the rotational symmetry axis of a charged cylindrical channel calculated by SPNP and by PNP approaches at different bulk ionic strengths. The height of curve peaks at $z=0$ (location of the channel center surrounded by the charged ring) indicates to what extent the electrostatic field of fixed charges is screened by the mobile ions. As expected, both SPNP and PNP results demonstrate better screening (lower peaks) at higher ionic strengths. In addition, neglect of ion desolvation inside the pore leads to better screening, resulting from an overestimation of the average negative charge accumulated in the channel and especially in proximity of the permanent charges. This result agrees well with the general understanding that the desolvation effect favours expulsion of ions from channel interior towards the bulk solution and thus induces a decrease in the effective ionic strength inside the channel.

Both SPNP (Fig. 7A) and PNP calculations (data not shown) reveal that along the $z$-axis the anion concentration reaches its maximum, $c_-^{\max}$, at $z=0$. Interestingly, the cation distribution has an apparent concentration minimum, $c_+^{\min}$, slightly shifted from the channel center towards the cathode, resembling in this way the SPNP results for the neutral channel (thick grey line in Fig. 4D). Similarly to the electrolyte polarization induced by external electrostatic field, an increase of the bulk ionic strength leads to a relatively weaker solution polarization (decrease of the ratio $c_-^{\max}/c_+^{\min}$) and to a rise in the total accumulated charge (increase of the

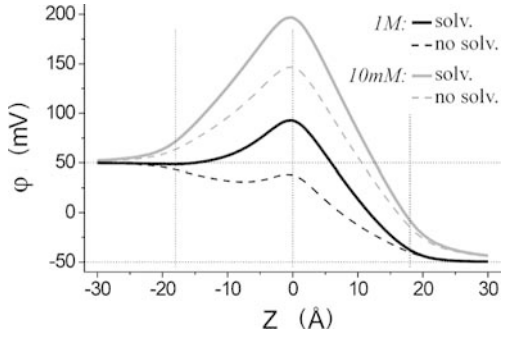


**Fig. 6** Electrostatic potential along the axis of a positively charged cylindrical channel with radius of 4 Å. *Black* and *grey lines* correspond to bulk ionic strengths of 1 M and 10 mM. Calculations with and without inclusion of solvation effects are represented by *solid* and *dashed lines*, respectively. *Vertical dotted lines* indicate the position of the membrane and the channel center (around which a charge of $+1e$ is distributed). *Horizontal dotted lines* show the boundary potentials used in the calculations

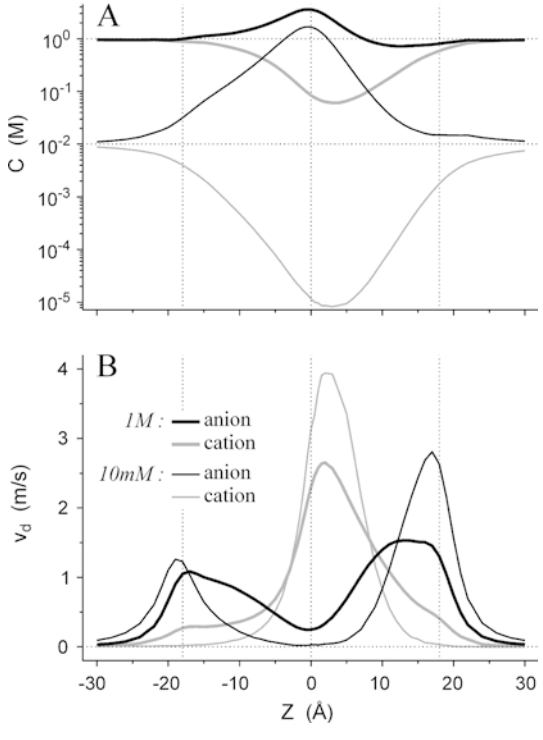


**Fig. 7** Longitudinal distributions of ion concentrations (**A**) and drift velocities (**B**) through the middle of a positively charged cylindrical channel with a radius of 4 Å. Calculations were performed with an external voltage of 100 mV. Solvation energies were included. *Grey* and *black solid lines* represent positive and negative ions, respectively, while *thick* and *thin lines* correspond to bulk concentrations of 1 M and 10 mM, respectively. *Vertical dotted lines* indicate the position of the membrane and the channel center (around which a charge of $+1e$ is distributed). *Horizontal dotted lines* show the bulk ion concentrations and $V_d = 0$

difference $c_- - c_+$). Inside the channel, the desolvation of mobile ions and the field of positive permanent charges have opposing effects on the population of anions and synergistically reduce the cation concentration. As a result, the relative rise in the concentration of positive ions is less than the relative drop in the negative ion concentration. In particular, $c_-^{max}/C_\pm^{bulk}$ is lower than $C_\pm^{bulk}/c_+^{min}$ by a factor of about 6.5 and 5.5 for bulk concentrations, $C_\pm^{bulk}$, of 10 mM and 1 M, respectively. In contrast, an omission of the solvation effect results in a symmetric rise/drop of the ion concentrations with respect to the bulk: $c_-^{max}/C_\pm^{bulk} \approx C_\pm^{bulk}/c_+^{min}$.

The steady state of the system presumes a conservation of the flow of a given ion type through channel cross-sections parallel to the membrane. This means that regions with high concentrations would be characterized by low drift velocities and $v$. As is seen from Fig. 7B, the computed drift velocity of negative ions shows a minimum at $z=0$ (the location of $c_-{}^{max}$) flanked by two maxima situated closely to the channel openings. This, however, does not mean that anions are necessarily slowed down at the channel center, as the drift velocity does not reflect the momentary speed of a particle. The longitudinal distribution of the cation $v_d$ has a single maximum with a location corresponding to $c_+{}^{min}$. At higher ionic strengths, velocity distributions in the channel interior tend be more uniform for both ion species. Similarly to simulations of neutral channels, PNP calculations for the charged cylindrical channel (results not presented) show more uniform velocity distributions compared to those resulting from SPNP and the space averaging yields $\langle v_{d(PNP)} \rangle$, which are slightly lower than the corresponding $\langle v_d \rangle$. Concentration and drift velocity profiles provide two equivalent, within the ergodic hypothesis, interpretations of one and the same phenomenon. For instance, elevated anion concentrations in the vicinity of the channel center means that at any given moment it is more probable to find an anion close to the pore center than in proximity of the openings. The minimum of $v_d$ versus $z$ at $z=0$, in turn, suggests that, on average, a negative ion would reside longer time in the central region than around the channel openings.

The two computational approaches, SPNP and PNP, showed significant differences in radial ion distributions. These differences were found to be most pronounced across the channel center, i.e. in the plane of the charged ring. At the channel center, both approaches gave practically equal anion concentrations, while calculated by the PNP method the cation concentration is about 6-fold higher than that obtained by the SPNP approach. Towards the channel wall, PNP simulations revealed an increase of $c_-$ and a reduction of $c_+$ (at $C_\pm{}^{bulk} = 10$ mM, the ratio $c^{wall}{}_{(PNP)}/c^{midd}{}_{(PNP)}$ is around 1.4 and 0.8 for negative and positive ions, respectively). In contrast, SPNP calculations showed weak a diminution of $c_-$ and a dramatic decrease of $c_+$ upon approaching the dielectric boundary of the pore (at $C_\pm{}^{bulk} = 10$ mM, $c^{wall}/c^{midd}$ was 0.9 and 0.13 for anions and cations, respectively). Evidently, the desolvation effect tends to focus the accumulated mobile charge in the middle of the pore. Omission of this effect results in an overestimation of both the solution charge density in proximity of protein charges (i.e. close to channel walls) and of the net mobile charge inside the channel.

It should be noted that the mean-field potential (solution of Eq. 7), on which PNP calculations are based, includes a reaction field of the dielectric media, improperly however, because this reaction field corresponds to a partial charge proportional to the average charge density $\Sigma_i Z_i e c_i$. The mean-field potential also includes components which presume that any ion placed at a certain point interacts with the average charge located at the very same point. This means that PNP simulations include some artificial unrealistic forces acting on mobile ions. For instance, in a region where $c_- > c_+$, those forces favour lowering of anion concentrations (as if desolvation is partially accounted) and stimulate a rise in cation concentrations (as if solvation energies of positive and negative ions differ in sign). Thus, the comparison between negative ion distributions calculated by PNP, $c_{-(PNP)}(\boldsymbol{r})$, and by SPNP, $c_-(\boldsymbol{r})$, showed that the relative difference between $c_{-(PNP)}(\boldsymbol{r})$ and $c_-(\boldsymbol{r})$ is smaller for a positively charged than for a neutral channel. For positive ions, however, the ratio $c_{+(PNP)}(\boldsymbol{r})/c_+(\boldsymbol{r})$, which is greater than 1 for the neutral pore, increases upon charging the channel. As a consequence, for the charged channel at 10 mM bulk ionic strength, PNP simulations gave a value of anion current, $I^-_{(PNP)}$, about 2-fold higher than $I^-$ calculated by SPNP, while for cation currents $I^+{}_{(PNP)}/I^+ \approx 12$ (in the case of neutral pore $I^+{}_{(PNP)}/I^+ = I^-_{(PNP)}/I^- = 5.2$). Since the total current through a charged channel is determined mainly by the flux of counter ions (anions in this case), the electric currents obtained by the two computational methods are in better agreement for charged than for neutral pores.

## Ion selectivity

As seen from Fig. 8, neglect of desolvation results in a significant underestimation of the ion selectivity of charged channels. A reduction of the pore radius leads to a stronger electrostatic field in the vicinity of the fixed charges as well as to a more distinct desolvation effect. Therefore, upon narrowing the channel, the ion selectivity rises; on the other hand, the difference between the selectivities calculated by the SPNP and the PNP approaches grows rapidly (Fig. 8A). Both types of electrodiffusion simulations showed that around physiological bulk ionic strengths (0.1 M) the selectivity of charged channels decreases almost linearly upon increasing the bath ion concentrations. At high bulk ion concentrations, for which the effective ionic strength in the channel interior is such that the corresponding Debye length becomes comparable to the channel radius, the dependence of selectivity on the ionic strength

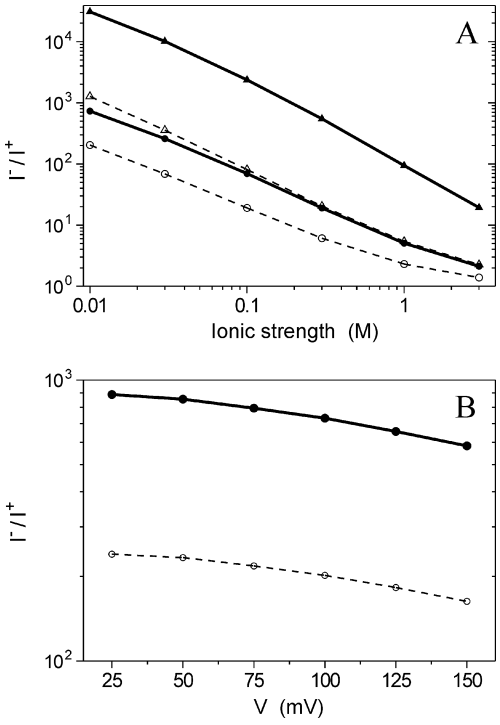


**Fig. 8A, B** Ion selectivity expressed as the ratio between anion and cation currents of positively charged cylindrical channels. **A** Dependence of selectivity on the ionic strength of a symmetric solution at 100 mV external voltage. Calculations were performed for channels with radii of 4 Å (*circles*) and 2 Å (*triangles*), with (*solid lines*,*filled symbols*) and without (*dashed lines*,*open symbols*) ion solvation.**B** Dependence of selectivity on the applied external voltage for channel with a 4 Å radius at 10 mM ionic strength

gradually vanishes and the channels tend to be non-selective. Calculations also demonstrated a weak but still notable reduction in ion selectivity upon increasing the external voltage (Fig. 8B). It seems that, in this case, channel selectivity arises from two competing factors: on one hand, the field of fixed charges, which acts as a selective filter, and on the other hand, the electric field of the electrodes supposing no selectivity.

## *I–V* curves

While the distributions of mobile ions and the electrostatic field inside a channel cannot be measured directly, techniques for measuring *I–V*characteristics are well developed and provide the most essential information for electrodiffusion properties of protein channels. That is why selectivity and conductivity are often the only basis for comparisons between theoretical models and experimental observations. For all channels studied in this work, simulations revealed that charged pores possess distinct selectivity and have lower resistance than neutral ones. This effect of lining charges on channel permeability is known and can be qualitatively predicted from general considerations. Theoretical approaches, however, allow a detailed quantitative analysis of the

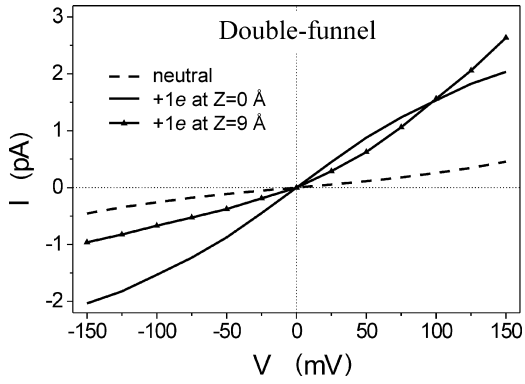


**Fig. 9** *I–V*characteristics calculated for a double-funnel channel with different fixed charge distributions: neutral (*dashed line*), charge of +1*e* at $Z = 0$ Å, i.e. surrounding the channel center (*solid line*), and at $Z = 9$ Å, i.e. 1/4 of the membrane thickness away from the center (*solid line* and *filled triangles*). Simulations were carried out with ion concentrations of 10 mM in both bath regions. Ion solvation was included. *Horizontal* and *vertical dotted lines* indicate zero current and zero external potential, respectively

role of different factors, such as pore shape and distribution of fixed charges, on particular channel features. The calculated *I–V* characteristic of the neutral double-funnel pore (Fig. 9, dashed line) was symmetric and almost linear, with a tendency of elevation of the conductance with increasing the magnitude of the external voltage. Positive and negative ions contribute equally to the total electric current. The introduction of fixed charges around the channel center (Fig. 9, solid line) led not just to a rise of the total electric current but also to a change in the form of the *I–V* curve, which, still being symmetric, indicates a decrease of the conductance upon rising the voltage. The symmetry of the current–voltage characteristic was lost when the charged ring was moved away from the center along *z*-axis. The most pronounced asymmetry was achieved for placing the charge about halfway between the channel center and one of its openings (Fig. 9, line marked with triangles), in which regions simulations of the neutral channel showed maximum density of mobile charge (maximum difference between black and grey thick lines in Fig. 4E). As could be expected, cation fluxes were found to be negligible in all positively charged channels.

The funnel pore provides another interesting example of how the interplay between the channel shape and the distribution of protein charges may produce non-linear and asymmetric current–voltage characteristics (Fig. 10). As is seen from Fig. 4F, I and L, even in absence of any fixed charges this pore shows significantly different electrodiffusion properties for ion species flowing in different directions. As a consequence, the neutral funnel-shaped channel manifests selectivity which is dependent on the polarity of the external voltage, so that the pore turns to be selective for ions entering from its wider opening. Thus, both cation and anion components of the current exhibit asymmetric current–voltage characteristics ("+" and "–" symbols in Fig. 10). However, cation and anion *I–V* curves are

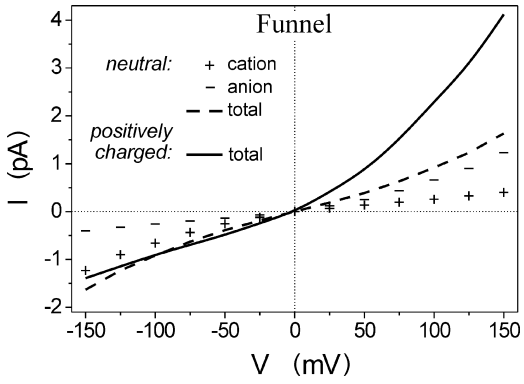


**Fig. 10** *I–V*characteristics of a neutral (*dashed line*) and a charged, $+1e$ at $Z=0$ Å (*solid line*), funnel-shaped channel. The contributions of fluxes of positive (+) and negative ions (–) to the total current through the neutral channel are also shown. Calculations were performed for symmetric solution of 10 mM salt concentration. Ion solvation was accounted. *Dotted lines* indicate zero current and zero external potential

symmetric to each other $[I^+(V)=-I^-(-V)]$, which results in a symmetric *I–V* curve for the total electric current (Fig. 10, dashed line). Placement of a positive charge around the pore center increases the anion component of the current and practically eliminates the cation flux, thus producing asymmetric current–voltage dependence (Fig. 10, solid line).

Charged channels embedded in asymmetric solutions usually yield asymmetric current–voltage characteristics with non-zero current in absence of external voltage. Our considerations clearly show that, at identical ion contents in the bath regions, there is no ion flux at $V=0$. However, depending mainly on the concrete pore form and protein charge distribution, asymmetric *I–V* curves may be reproduced. Additional simulations demonstrated that the selectivity and *I–V*characteristics of channels can be modulated by other factors like differences in radii and/or diffusion coefficients of ion species.

## Conclusions

The computational method proposed in this work represents an extension of the continuum approaches based on the PNP theory. Although the method does not overstep the limitations typical for continuum models, it allows the electrodiffusion properties of any protein channel with known structure to be scrutinized on an atomic level. This was achieved by a modification of the PNP theory regarding a more accurate consideration of ion sizes and desolvation effects in the pore region.

The advantages of the present model can be summarized as follows. (1) It provides realistic results for narrow channels, where previous PNP approaches either fail or employ excess chemical potential as a justifiable parameter. (2) The method yields distribution profiles of mobile ions which are in accord with the predictions of BD simulations (Chung et al. 1998; Dieckmann et al. 1999; Corry et al. 2000, 2001). (3) Non-linearity and asymmetry of *I–V* curves, as well as ion selectivity and its dependence on channel architecture and ionic strength, are adequately reflected. These features of the computational method make us to believe that it, together with the computer code which will be available on request, can be a useful tool for analysis of the properties of a wide variety of membrane channels.

**Acknowledgements** U.Z. thanks EMBO for a short-term fellowship, ASTF 9864.

## References

Alexov E, Gunner MR (1997) Incorporating protein conformational flexibility into the calculation of pH-dependent protein properties. Biophys J 72:2075–2093

Allen TW, Kuyucak S, Chung H (2000) Molecular dynamics estimates of ion diffusion in model hydrophobic and KcsA potassium channels. Biophys Chem 86:1–14

Boda D, Busath DD, Henderson D, Sokolowski S (2000) Monte Carlo simulations of the mechanism of channel selectivity: the competition between volume exclusion and charge neutrality. J Phys Chem B 104:8903–8910

Boda D, Henderson D, Busath DD (2001) Monte Carlo study of the effect of ion and channel size on the selectivity of a model calcium channel. J Phys Chem B 105:11574–11577

Cardenas AE, Coalson RD, Kurnikova MG (2000) Three-dimensional Poisson-Nernst-Planck theory studies: Influence of membrane electrostatics on gramicidin A channel conductance. Biophys J 79:80–93

Chung SH, Hoyles M, Allen T, Kuyucak S (1998) Study of ionic currents across a model membrane channel using Brownian dynamics. Biophys J 75:793–809

Corry B, Kuyucak S, Chung SH (2000) Tests of continuum theories as models of ion channels. II. Poisson-Nernst-Planck theory versus Brownian dynamics. Biophys J 78:2364–2381

Corry B, Allen TW, Kuyucak S, Chung SH (2001) Mechanisms of permeation and selectivity in calcium channels. Biophys J 80:195–214

Dieckmann GR, Lear JD, Zhong QF, Klein ML, DeGrado WF, Sharp KA (1999) Exploration of the structural features defining the conduction properties of a synthetic ion channel. Biophys J 76:618–630

Dillet V, van Etten RL, Bashford D (2000) Stabilization of charges and protonation state in the active site of the protein tyrosine phosphatases: a computational study. J Phys Chem B 104:11321–11333

Eisenberg RS (1996) Computing the field in proteins and membranes. J Membr Biol 150:1–25

Gillespie D, Eisenberg R (2001) Modified Donnan potentials for ion transport through biological ion channels. Phys Rev E 63:061902-0611-7

Gillespie D, Eisenberg RS (2002) Physical descriptions of experimental selectivity measurements in ion channels. Eur Biophys J 31:454–466

Gilson M, Sharp KA, Honig BH (1987) Calculating electrostatic potential of molecules in solution: method and error assessment. J Comput Chem 9:327–335

Goulding D, Hansen JP, Melchionna S (2000) Size selectivity of narrow pores. Phys Rev Lett 85:1132–1135

Goulding D, Melchionna S, Hansen JP (2001) Entropic selectivity of microporous materials. Phys Chem Chem Phys 3:1644–1654

Graf P, Nitzan A, Kurnikova MG, Coalson RD (2000) A dynamic lattice Monte Carlo model of ion transport in inhomogeneous dielectric environments: method and implementation. J Phys Chem B 104:12324–12338

Gummel HK (1964) A self-consistent iterative scheme for one-dimensional steady state transistor calculations. IEEE Trans Electron Devices ED-11:455–465

Gunner MR, Alexov E (2000) A pragmatic approach to structure based calculation of coupled proton and electron transfer in proteins. Biochim Biophys Acta 1458:63–87

Hadjidimos A (2000) Successive overrelaxation (SOR) and related methods. J Comp Appl Math 123:177–199

Hollerbach U, Chen D, Nonner W, Eisenberg B (1999) Three dimensional Poisson-Nernst-Planck theory of open channels. Biophys J 76:A205

Hollerbach U, Chen DP, Busath DD, Eisenberg B (2000) Predicting function from structure using the Poisson-Nernst-Planck equations: sodium current in the gramicidin A channel. Langmuir 16:5509–5514

Jerome JW (1996) Analysis of charge transport: a mathematical study of semiconductor devices. Springer, Berlin Heidelberg New York

Karshikoff A (1995) A simple algorithm for calculation of multiple site titration curves. Protein Eng 8:243–248

Karshikoff A, Spassov V, Cowan RQ, Ladenstein R, Schirmer T (1994) Electrostatic analysis of two porin channels from *E. coli*. J Mol Biol 240:372–384

Koumanov A, Rüterjans H, Karshikoff A (2002) Continuum electrostatic analysis of irregular ionization and proton allocation in proteins. Proteins 46:85–96

Koumanov A, Benach J, Atrian S, Gonzàlez-Duarte R, Karshikoff A, Ladenstein R (2003) The catalytic mechanism of *Drosophila* alcohol dehydrogenase: evidence for a proton relay modulated by the coupled ionisation of the active site lysine/tyrosine pair and a NAD+ ibose OH switch. Proteins (in press)

Kurnikova MG, Coalson RD, Graf P, Nitzan A (1999) A lattice relaxation for three-dimensional Poisson-Nernst-Planck theory with application to ion transport through the gramicidin A channel. Biophys J 76:642–656

Levitt DG (1999) Modeling of ion channels. J Gen Physiol 113:789–794

Moy G, Corry B, Kuyucak S, Chung,S H (2000) Tests of continuum theories as models of ion channels. I. Poisson-Boltzmann theory versus Brownian dynamics. Biophys J 78:2349–2363

Nicholls A, Honig B (1991) A rapide finite difference algorithm, utilizing successive over-relaxation to solve the Poisson-Boltzmann equation. J Comput Chem 12:435–445

Nonner W, Eisenberg B (1998) Ion permeation and glutamate residues linked by Poisson-Nernst-Planck theory in L-type calcium channels. Biophys J 75:1287–1305

Nonner W, Chen DP, Eisenberg B (1998) Anomalous mole fraction effect, electrostatics, and binding in ionic channels. Biophys J 74:2327–2334

Nonner W, Chen DP, Eisenberg B (1999) Progress and prospects in permeation. J Gen Physiol 113:773–782

Nonner W, Catacuzzeno L, Eisenberg B (2000) Binding and selectivity in L-type Ca channels: a mean spherical approximation. Biophys J 79:1976–1992

Nonner W, Gillespie D, Henderson D, Eisenberg B (2001) Ion accumulation in a biological calcium channel: effects of solvent and confining pressure. J Phys Chem B 105:6427–6436

Partenskii MB, Jordan PC (1992) Theoretical perspectives on ion-channel electrostatics: continuum and microscopic approaches. Q Rev Biophys 25:477–510

Riveros O, Croxton T, Armstrong WMD (1989) Liquid junction potentials calculated from numerical solutions of the Nernst-Planck and Poisson equations. J Theor Biol 140:221–230

Robinson RA, Stokes RH (1959) Electrolyte solutions: the measurement and interpretation of conductance, chemical potential and diffusion in solutions of simple electrolytes, 2nd edn. Butterworths, London

Roux B (2002) Theoretical and computational models of ion channels. Curr Opin Struct Biol 12:182–189

Sansom MSP, Smith GR, Adcock C, Biggin PC (1997) The dielectric properties of water within model transbilayer pores. Biophys J 73:2404–2415

Sartoris G (1998) A 3D rectangular mixed finite element method to solve the stationary semiconductor equations. SIAM J Sci Comput 19:387–403

Schuss Z, Nadler B, Eisenberg RS (2001) Derivation of Poisson and Nernst-Planck equations in a bath and channel from a molecular model. Phys Rev E 64:036116

Selberherr S (1984) Analysis and simulation of semiconductor devices. Springer, Berlin Heidelberg New York

Smith GR, Sansom MSP (1999) Effective diffusion coefficients of $K^+$ and $Cl^-$ ions in ion channel models. Biophys Chem 79:129–151

Tieleman D, Berendsen H (1998) A molecular dynamics study of the pores formed by*Escherichia coli* OmpF porin in a fully hydrated palmitoyloleoylphosphatidylcholine bilayer. Biophys J 74:2786–2801

Tieleman DP, Biggin PC, Smith GR, Sansom MSP (2001) Simulation approaches to ion channel structure–function relationships. Q Rev Biophys 34:473–561

Voges D, Karshikoff A (1998) A model for a local static dielectric constant in macromolecules. J Phys Chem 108:2219–2227

Warwicker J, Watson NC (1982) Calculation of the electric field potential in the active site cleft due to alpha-helix dipoles. J Mol Biol 157:671–679

Zachariae U, Koumanov A, Engelhardt H, Karshikoff A (2002) Electrostatic properties of the anion selective porin Omp32 from *Delftia acidovorans* and of the arginine cluster of bacterial porins. Protein Sci 11:1309–1319